Effects of a High Magnetic Field on the Microstructure of Ni-Based Single-Crystal Superalloys During Directional Solidification

WEIDONG XUAN, JIAN LAN, HUAN LIU, CHUANJUN LI, JIANG WANG, WEILI REN, YUNBO ZHONG, XI LI, and ZHONGMING REN

High magnetic fields are widely used to improve the microstructure and properties of materials during the solidification process. During the preparation of single-crystal turbine blades, the microstructure of the superalloy is the main factor that determines its mechanical properties. In this work, the effects of a high magnetic field on the microstructure of Ni-based single-crystal superalloys PWA1483 and CMSX-4 during directional solidification were investigated experimentally. The results showed that the magnetic field modified the primary dendrite arm spacing, γ' phase size, and microsegregation of the superalloys. In addition, the size and volume fractions of γ/γ' eutectic and the microporosity were decreased in a high magnetic field. Analysis of variance (ANOVA) results showed that the effect of a high magnetic field on the microstructure during directional solidification was significant ($p < 0.05$). Based on both experimental results and theoretical analysis, the modification of microstructure was attributed to thermoelectric magnetic convection occurring in the interdendritic regions under a high magnetic field. The present work provides a new method to optimize the microstructure of Ni-based single-crystal superalloy blades by applying a high magnetic field.

DOI: 10.1007/s11661-017-4135-5

I. INTRODUCTION

Ni-BASED superalloy single-crystal turbine blades have been used in advanced aero-engines and industrial gas turbines (IGTs) because of their excellent high-temperature strength and creep resistance. These favorable mechanical properties of single-crystal turbine blades are derived from their elimination of grain boundaries.[1,2] Therefore, the microstructure of a single-crystal blade is an important factor determining its mechanical properties.[3–5] In industrial production, single-crystal turbine blades of Ni-based superalloys are usually produced through the Bridgman high rate solidification method.[6,7] However, to ensure the formation of suitable single-crystal turbine blades, especially for use in IGTs, a low solidification velocity is needed during directional solidification. As a consequence, the single-crystal blades contain coarse dendrite spacing and high element segregation, which degrade their mechanical properties.[8,9] Recently, many novel methods such as liquid metal cooling (LMC),[10–12] gas cooling casting (GCC),[13] zone melting liquid metal cooling (ZMLMC),[5] and downward directional solidification (DWDS)[14] have been developed to optimize the microstructure of single-crystal superalloys and enhance their mechanical properties. However, when these processes are used to produce single-crystal blades for IGTs, some disadvantageous effects occur, such as casting contamination,[15] furnace temperature decrease, grain defect formation,[3,14] non-homogeneous thermal field, and stray grain production.[16,17] These effects degrade the mechanical properties of superalloys.

Recently, external high magnetic fields have been used to modify the solidification microstructure of alloys, such as the dendrite and inter-lamellar spacing,[18–20] phase transformation temperature,[18] solute distribution,[20,21] and solidification rate.[22] Our previous work indicated that a high magnetic field increased the dendrite number and decreased the dendrite arm spacing in directionally solidified superalloy DZ417G.[23–25] We also found that the effect of the magnetic field on microstructure originated from thermoelectric magnetic convection and stress. However, the thermoelectric magnetic convection and stress induced by the high magnetic field may drive the formation of higher-order dendrites from primary dendrites and cause the

WEIDONG XUAN, JIAN LAN, HUAN LIU, CHUANJUN LI, JIANG WANG, WEILI REN, YUNBO ZHONG, XI LI, and ZHONGMING REN are with the State Key Laboratory of Advanced Special Steel & Shanghai Key Laboratory of Advanced Ferrometallurgy & School of Materials Science and Engineering, Shanghai University, Shanghai 200072, P. R. China. Contact e-mail: wdxuan@shu.edu.cn

Manuscript submitted October 12, 2016.
Article published online May 15, 2017

detachment of dendrite arms.[23–26] Moreover, some investigations have indicated that both the detachment of dendrite arms and formation of higher-order dendrites are the factors that increase the dendrite number and decrease the dendrite arm spacing in directionally solidified superalloys.[10,26–28] It is still not clear what causes the increase of dendrite number and decrease of dendrite arm spacing in directionally solidified superalloys under high magnetic fields. Therefore, it is necessary to thoroughly explore the evolution mechanism of the microstructure of Ni-based superalloys under high magnetic fields.

The objective of this study is to investigate the effects of a high magnetic field on the microstructures of single-crystal superalloy PWA1483 and CMSX-4 during directional solidification. The results show that the magnetic field causes the primary dendrite arm spacing, γ' phase size, and microsegregation to decrease. In addition, the size and volume fractions of γ/γ' eutectic and microporosity decrease under a high magnetic field. These results may be attributed to thermoelectric magnetic convection occurring in the interdendritic regions under a high magnetic field.

II. EXPERIMENTAL METHODS

The alloys used here were Ni-based single-crystal superalloys PWA1483 and CMSX-4. The chemical composition of PWA1483 was Cr 12.2, Co 9.0, Mo 1.9, W 3.8, Al 3.6, Ti 4.2, Ta 5.0, and C 0.07 (wt pct), with Ni as the balance. The chemical composition of CMSX-4 was Cr 6.5, Co 9.0, Mo 0.6, W 6.0, Al 5.6, Ti 4.7, Ta 6.5, and Re 3.0 (wt pct), with Ni as the balance. Each single-crystal sample was produced using a seeding technique in a directional solidification furnace. Seeds of superalloy PWA1483 and CMSX-4 were placed at the bottom of the mold to control the grain number and orientation of crystals in superalloy PWA1483 and CMSX-4, respectively.

The directional solidification apparatus under a high magnetic field ($B > 2$ *T*) is depicted schematically in Figure 1.[25] The apparatus mainly consisted of a superconducting magnet, Bridgman-type furnace with a withdrawal system, and temperature controller. The superconducting magnet could produce a vertical static magnetic field with a maximum intensity of 14 *T*. The maximum furnace temperature was 1973 K (1700 °C) with a precision of ±1 K. A liquid Ga-In-Sn metal (LMC) pool with a water cooling jacket was used to cool the sample. The temperature gradient in the sample was controlled by adjusting the temperature of the furnace hot zone, which was isolated from the LMC by a refractory baffle. The withdrawal velocity was controlled by a withdrawing device and could be continuously adjusted between 0.5 and 10,000 μm/s.

During the experiments, each sample was heated to 1823 K (1550 °C) and held at this temperature for 30 minutes to partially melt the seed crystal, and then directionally solidified in the Bridgman apparatus by withdrawing the crucible assembly downward at a constant withdrawal velocity. After the casting experiment, the transverse (perpendicular to the solidification direction) microstructures of samples obtained from experiments were examined after etching by a Leica optical microscope to study the primary dendrite arm spacing, γ/γ' eutectic, and microporosity. The etchant solution was composed of $CuSO_4$ (4 g), HCl (20 mL), H_2SO_4 (12 mL), and H_2O (25 mL). The crystal orientations of grains were investigated by electron backscatter diffraction technology. A scanning electron microscope (SEM) was used to study the γ' phase in the samples. The solute distributions in the dendrite core and interdendritic regions were measured by a field-emission SEM equipped with an energy-dispersive X-ray spectrometer (EDS).

The primary dendrite arm spacing was measured by the area counting method for the transverse sections using the equation $\lambda = (A/N)^{0.5}$, where A is the area of the selected region and N is the average number of primary dendrites in A. The volume fractions of γ/γ' eutectic and microporosity were determined by the metallographic analytical software Image Pro Plus. The size of the γ' phase was evaluated using $A = (S_T/M)^{0.5}$, where S_T is the cumulative total γ' area in the viewing field of a micrograph (in the dendrite core), and M is the number of γ' phase.

III. RESULTS

A. *Primary Dendrite Arm Spacing*

Figure 2 shows the transverse microstructures of samples during directional solidification of the two superalloys at a withdrawal velocity of 50 μm/s without and with a 5 *T* magnetic field. In the case of no magnetic field, coarse primary dendrite spacing is observed (Figures 2(a) and (b)). However, when the high magnetic field is applied during directional solidification, the primary dendrite spacing is refined, as illustrated in Figures 2(c) and (d). The changes of the primary dendrite arm spacing without and with a high magnetic field were measured. The results are listed in Table I. Compared with the case without a magnetic field, the primary dendrite arm spacing of superalloys PWA1483 and CMSX-4 decreased from 260 to 180 μm (30 pct) and from 290 to 230 μm (20 pct) under a 5 *T* magnetic field, respectively. This means that the high magnetic field refines the primary dendrite spacing during directional solidification under the present experimental conditions.

B. *γ' Precipitate Phase*

Figure 3 displays the γ' phase morphologies in the dendrite cores produced in samples without and with an applied high magnetic field. A finer γ' phase is obtained under the applied magnetic field, as shown in Figures 3(c) and (d). The average sizes of the γ' phase in the samples produced without and with the magnetic field were measured. The results are presented in Table I. Compared with the γ' phase formed without the magnetic field, a 5 *T* magnetic field decreases the γ'

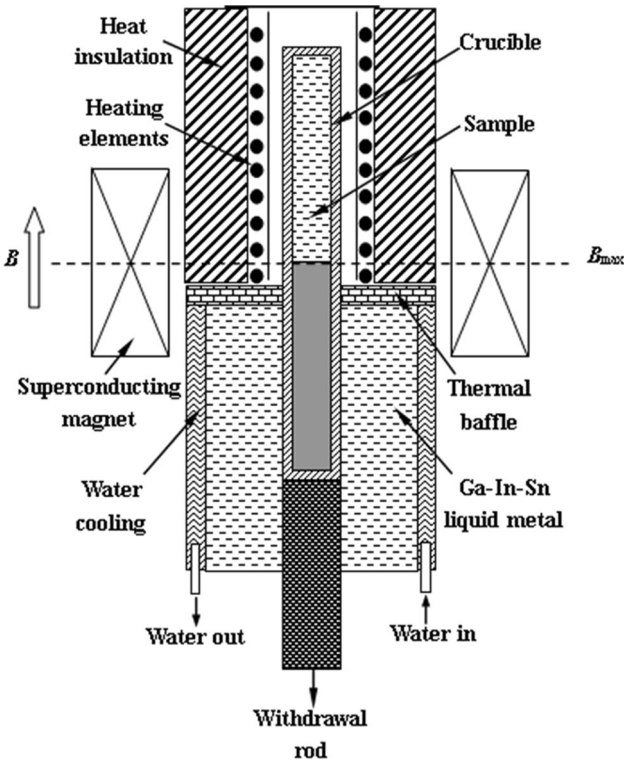

Fig. 1—Schematic of the Bridgman solidification apparatus in the superconducting magnet.[25]

phase size by 46 and 40 pct for superalloy PWA1483 and CMSX-4, respectively.

C. γ/γ' *Eutectic*

Figure 4 shows the morphologies of the γ/γ' eutectic of samples during directional solidification of the superalloys at a withdrawal velocity of 50 μm/s without and with a 5 T magnetic field. For both types of superalloy, a large block-like γ/γ' eutectic is observed without the applied magnetic field. However, when a high magnetic field is applied, a smaller γ/γ' eutectic phase is obtained. The average volume fractions of γ/γ' eutectic without and with the magnetic field are given in Table I. The applied magnetic field decreases the content of γ/γ' eutectic by about 49 and 44 pct for superalloy PWA1483 and CMSX-4, respectively.

D. *Microporosity*

The microporosity in transverse sections of the directionally solidified samples obtained at a withdrawal velocity of 50 μm/s without and with a 5 T magnetic field are provided in Figure 5. The high magnetic field decreases the microporosity size. The volume fraction of microporosity in Figure 5 was measured, and was listed in Table I. These results indicate that the volume fraction and size of microporosity are decreased in the presence of a high magnetic field compared with those obtained without an applied magnetic field.

IV. DISCUSSIONS

The above experimental results reveal that the applied high magnetic field modifies the primary dendrite arm spacing and size of the γ' phase for both superalloys. Moreover, the size and volume faction of γ/γ' eutectic and microporosity are changed by the magnetic field. ANOVA analysis was used to investigate the influences of the high magnetic field and alloy type on the microstructures of superalloys using the normalized values obtained using the mean values in Table I. The normalized values were included as repeated measures in the ANOVA analysis. The results of ANOVA analysis are presented in Table II and indicate that the effect of the applied magnetic field is significant ($p = 0.0001$), while the effect of the alloy type is slightly significant ($p = 0.0426$). Meanwhile, the p value of the interaction term (X1·X2) is well above the 0.05 threshold ($p = 0.8259$), which indicates that the high magnetic field affects alloys in a common way regardless of the alloy type. In addition, ANOVA analyses were carried out for every microstructural feature, including primary dendrite arm spacing, gamma prime precipitate size, eutectic volume fraction, and microporosity. These analyses also indicated that the high magnetic field has a significant effect on each of these microstructural features. When a high magnetic field is applied during directional solidification, the magnetic field has two main effects on the microstructure: one effect is that the electromagnetic braking (EMB) arising from the interaction between the moving conducting melt and magnetic field will suppress the natural convection;[29–31] the other effect is that a thermoelectric magnetic force (TEMF) in the solid phase and the thermoelectric magnetic convection (TEMC) in the liquid phase will be formed because of the thermoelectric magnetohydrodynamics (TEMHD) derived from the interaction between the thermoelectric current and magnetic field.[32–34] The TEMC will induce melt convection, while the TEMF will produce a force in the dendrites.

When a high magnetic field is applied during directional solidification, EMB and TEMC affect the melt flow simultaneously. Li *et al.*[35] investigated the relationship between EMB and TEMC and the magnitudes of TEMC at different scales. They found that the fluid velocity increases as $B^{1/2}$ in a low magnetic field and then decreases as B^{-1} in a high magnetic field. When the intensity of the applied magnetic field reaches a critical value, the TEMC is balanced with the viscous friction and EMB, and the fluid velocity reaches its maximum value. The critical magnetic field intensity B_{max} is

$$B_{max} = \left(\frac{\rho(S_S - S_L)G}{l\sigma}\right)^{1/3}, \quad [1]$$

where ρ is the density of the alloy liquid; S_L and S_S are the thermoelectric powers of the liquid and solid, respectively; l is the typical length scale; and σ is electrical conductivity. B_{max} was estimated based on Eq. [1]. According to the corresponding physical parameters of the Ni-based superalloys presented in Table III, B_{max} was 5.4 T. This calculated result suggests that TEMC plays an

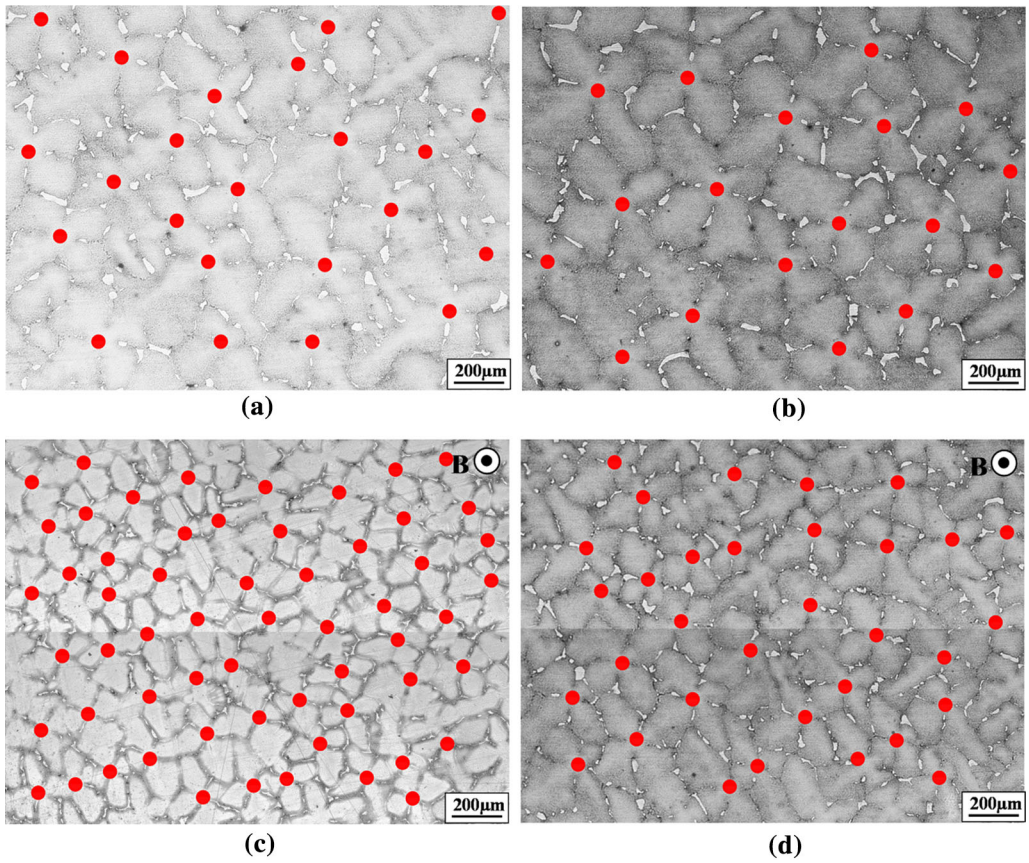

Fig. 2—Transverse microstructures of superalloy PWA1483 and CMSX-4 without and with a 5 *T* magnetic field. The primary dendrite cores are indicated by red dots: (*a*) PWA1483, 0 *T*; (*b*) CMSX-4, 0 *T*; (*c*) PWA1483, 5 *T*; (*d*) CMSX-4, 5 *T*.

Table I. Microstructural Features of Superalloys

Alloy	PWA1483		CMSX-4	
Magnetic Field Intensity (*T*)	0	5	0	5
Primary dendrite arm spacing (μm)	260	180	290	230
γ′ precipitate phase size (nm)	450	250	600	360
γ/γ′ eutectic volume fraction (pct)	1.92	1.06	2.3	1.34
Microporosity volume fraction (pct)	0.12	0.02	0.15	0.04

important role in the solidification process under the current experimental conditions ($B \leq 5$ *T*).

In addition, when a magnetic field is applied during directional solidification, a TEMF will act on the dendrites, which is given by

$$F_{\text{TEMF}} = \frac{-\sigma_{\text{L}}\sigma_{\text{S}}f_{\text{L}}}{\sigma_{\text{L}}f_{\text{L}} + \sigma_{\text{S}}f_{\text{S}}}(S_{\text{S}} - S_{\text{L}})\nabla TB, \qquad [2]$$

where σ_{L} and σ_{S} are the electrical conductivities of the liquid and solid, respectively; f_{L} and f_{S} are the liquid and solid fractions, respectively. Equation [2] shows that the TEMF in the solid increases linearly with rising magnetic field intensity.

According to Li *et al.*,[40] a TEMF of the order of 10^5 N/m^3 is strong enough to break down dendrites. To investigate the effect of the TEMF on dendrites during directional solidification, the magnitudes of the TEMF in dendrites under various magnetic fields were evaluated, as shown in Figure 6. When the magnetic field is higher than 3.5 *T*, the TEMF is larger than 10^5 N/m^3. This result suggests that the TEMF under a 5 *T* magnetic field is strong enough to break down dendrites. However, the present experimental results indicate that a 5 *T* high magnetic field does not induce the deformation, fracture, or deflection of dendrites and a single-crystal sample is obtained from directional solidification, as illustrated in Figure 7. Therefore, according to the above analyses, the change of the microstructures of the superalloys during directional solidification should be attributed to the TEMC induced in a high magnetic field.

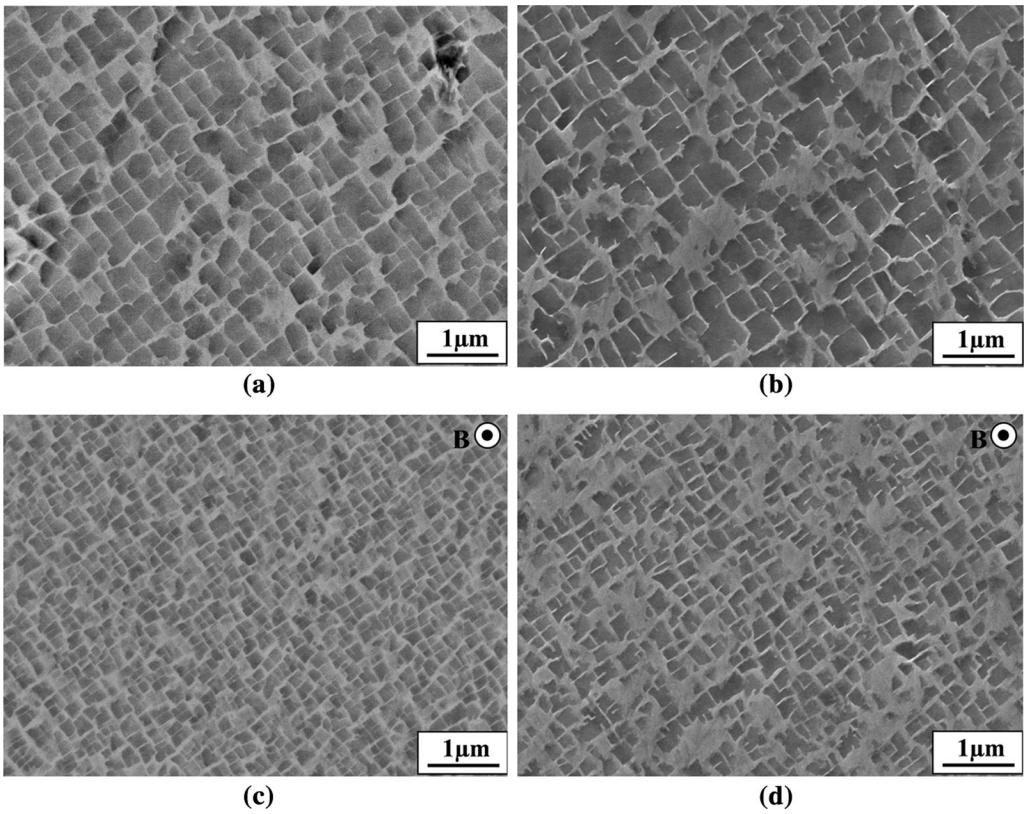

Fig. 3—Morphologies of the γ' phase in the dendrite core of superalloy PWA1483 and CMSX-4 without and with a 5T magnetic field: (*a*) PWA1483, 0 *T*; (*b*) CMSX-4, 0 *T*; (*c*) PWA1483, 5 *T*; (*d*) CMSX-4, 5 *T*.

A. *Influence of TEMC on Primary Dendrite Arm Spacing and Microporosity*

Recently, some investigations have indicated that for a given alloy with the same thermal gradient (G) and cooling rate (V), convection is an important factor that affects primary dendrite arm spacing during directional solidification.[28,41–43] Indeed, the primary dendrite arm spacing decreases under natural[28,41] or forced convection.[42,43] To reveal the effect of melt flow on the primary dendrite arm spacing during directional solidification, a series of experiments was conducted.[44–46] It was found that the change of primary dendrite arm spacing is closely related to the interdendritic constitutional undercooling during directional solidification. Enhancing the degree of interdendritic undercooling induces the growth of tertiary dendrites and refinement of the primary dendrite arm spacing. According to Curreri *et al.*,[47] the natural convection arising from the density difference can cause the magnitude of interdendritic constitutional undercooling to increase. Considering the present experimental results, one possible explanation is that when a high magnetic field is applied during directional solidification of the superalloys, an interdendritic TEMC is formed that causes interdendritic constitutional undercooling to increase, which then drives the growth of tertiary dendrites. As a consequence, the primary dendrite arm spacing should decrease in a high magnetic field.

Solidification shrinkage is a major factor that causes the formation of microporosity, which are solidification defects that affect the mechanical performance of the casting.[3,10] It is well known that the formation of microporosity arises from the solidification shrinkage of the residual liquid in the interdendritic region during directional solidification. According to solidification principles, melt flow will increase the liquid feed into the interdendritic region and further decrease the size of microporosity. Likewise, when a high magnetic field is applied during directional solidification, the TEMC will cause melt flow and promote the liquid feed into the interdendritic region. As a consequence, small microporosity is formed in a high magnetic field. In addition, an investigation has shown that the final eutectic liquid fraction and primary dendrite arm spacing are the main factors that affect the formation of microporosity, which is[48]

$$d_{\text{pore}} = \frac{f_1 \lambda}{2}, \qquad [3]$$

where f_1 is the final eutectic liquid fraction, λ is the primary dendrite arm spacing. According to Eq. [3], the size of microporosity decreases as the decrease of primary dendrite arm spacing. The present experimental results indicate that the interdendritic TEMC induced by a high magnetic field causes the primary dendrite arm spacing to decrease. Thus, compared

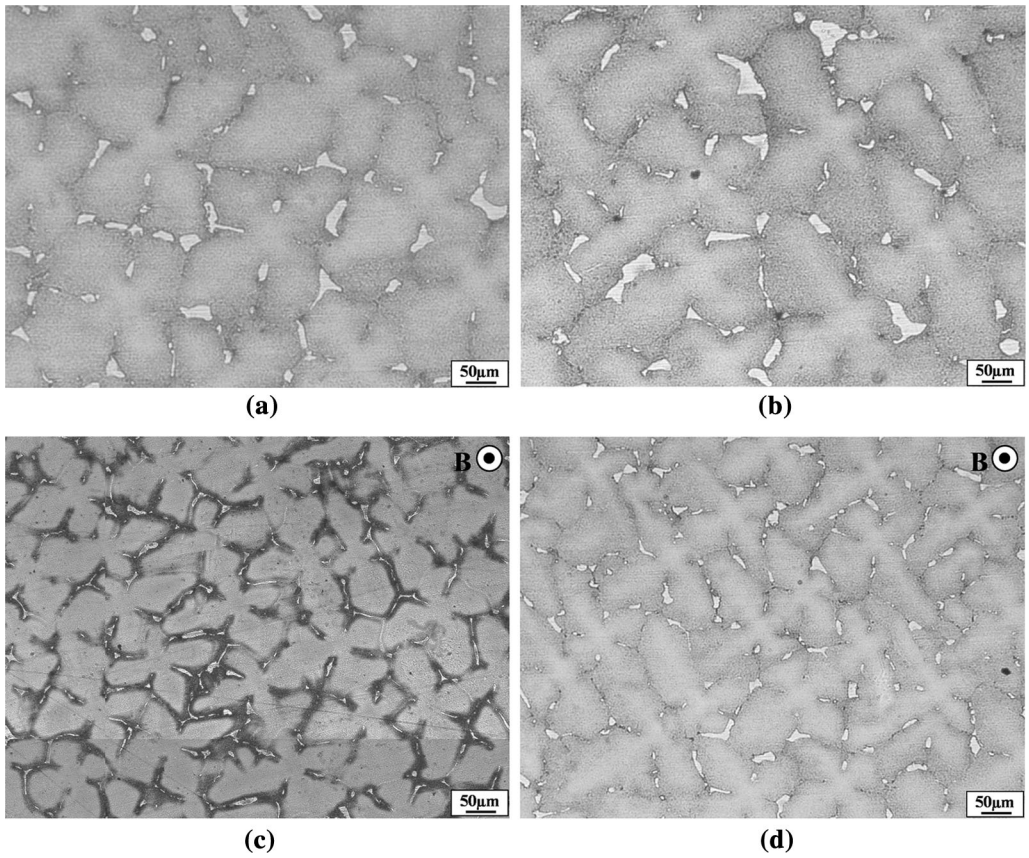

Fig. 4—Morphologies of γ/γ' eutectic of PWA1483 and CMSX-4 without and with a 5T magnetic field: (*a*) PWA1483, 0 *T*; (*b*) CMSX-4, 0 *T*; (*c*) PWA1483, 5 *T*; (*d*) CMSX-4, 5 *T*.

Table II. ANOVA Analysis of Magnetic Field, Alloy, and Four Microstructural Features

Parameter	SS	DF	MS	*F* Value	*p* Value
X1*	0.24125	1	0.24125	5.15	0.0426
X2**	1.74816	1	1.74816	37.29	0.0001
X1·X2	0.00237	1	0.00237	0.05	0.8259
Error	0.56262	12	0.04688		
Total	2.5544	15			

* X1 represents alloy
** X2 represents magnetic field.

Table III. Physical Parameters of the Ni-Based Superalloy.[36–39]

Physical Parameters	Magnitude
Electrical conductivity of solid (σ_S, Ω^{-1} m^{-1}) 1600 K (1327 °C)	0.75×10^6
Electrical conductivity of liquid (σ_L, Ω^{-1} m^{-1}) 1600 K (1327 °C)	0.67×10^6
Thermoelectric power of solid (S_S, μV K^{-1}) 1143 K (870 °C)	−10.95
Thermoelectric power of liquid (S_L, μV K^{-1}) 1773 K (1500 °C)	−16
Density of liquid alloy (ρ, Kg m^{-3}) 1613 K (1340 °C)	7.85×10^3

with the case without a magnetic field, smaller microporosity is formed in a high magnetic field. Therefore, the interdendritic TEMC induced in the high magnetic field should also be responsible for the decrease of microporosity size during directional solidification.

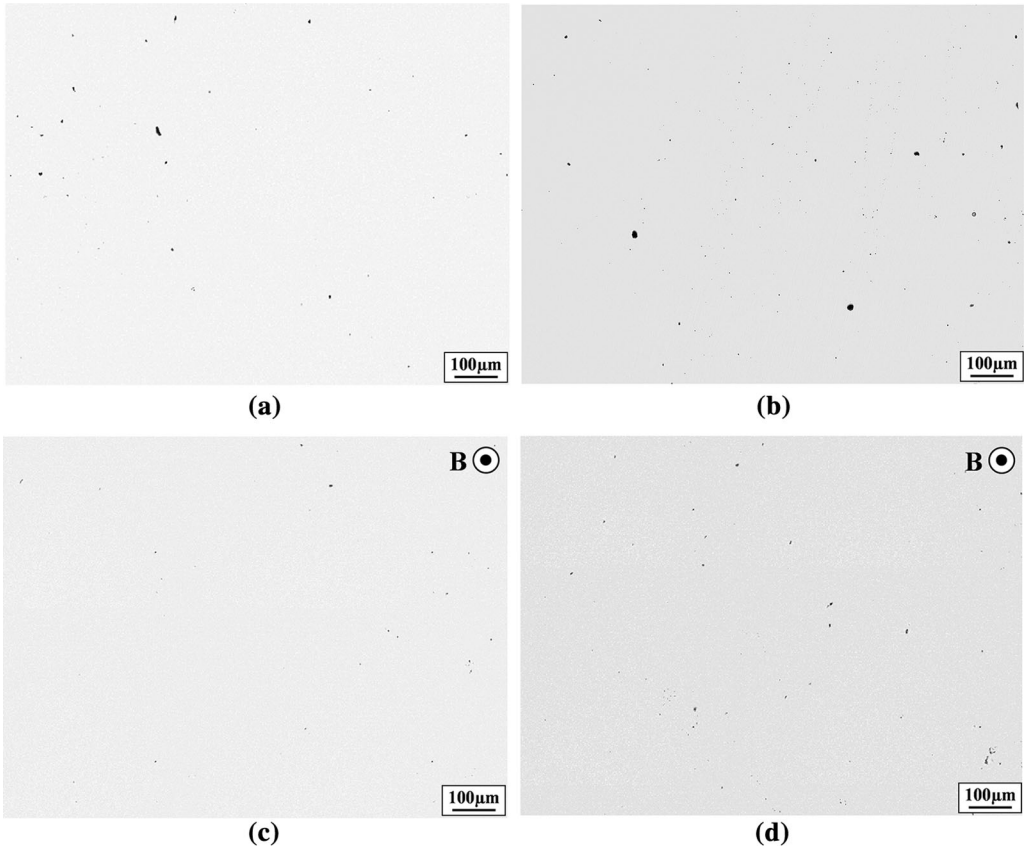

Fig. 5—Optical images of transverse sections of samples produced from PWA1483 and CMSX-4 without and with a 5 *T* magnetic field. Microporosity is shown as dark voids in the superalloys: (*a*) PWA1483, 0 *T*; (*b*) CMSX-4, 0 *T*; (*c*) PWA1483, 5 *T*; (*d*) CMSX-4, 5 *T*.

B. *Influence of TEMC on the γ′ Precipitate Phase and γ/γ′ Eutectic*

The γ' phase is a primary strengthening phase of superalloys, forming a coherent precipitate from the γ matrix phase during the solidification process, which can be written as

$$\gamma_1 \rightarrow \gamma_2 + \gamma', \qquad [4]$$

where γ_1 is the original γ solid solution, γ_2 is the residual γ solid solution, and γ' is the precipitate phase. The corresponding activation energy of nucleation ΔG^*[49] can be expressed as

$$\Delta G^* = \frac{16\pi\sigma^3_{\gamma-\gamma'}}{3(\Delta G_V - \Delta G_\varepsilon)^2} \qquad [5]$$

where ΔG_V is the difference in bulk Gibbs free energy between the γ and γ' phases, ΔG_ε is the difference in strain free energy for precipitation per unit volume of the γ' phase, and $\sigma_{\gamma-\gamma'}$ is the γ–γ' interfacial energy.

According to Xiao *et al.*[49] and Guo *et al.*,[50] the γ–γ' interfacial energy and the strain energy are the main factors affecting the shape of the γ' phase. The driving force for the nucleation of the γ' phase is the difference in bulk Gibbs free energy between the γ and γ' phases. However, the present experimental results indicate that the size of the γ' phase is changed by the applied magnetic field, but the shape of the γ' phase is not. According to the above analyses, it is deduced that the effect of a high magnetic field on the bulk Gibbs free energy during the solidification process is the main reason for the change of the size of the γ' phase under the present experimental conditions. Yamaguchi and Tanimoto[51] investigated the effect of a high magnetic field on thermodynamic constants, and found that the thermodynamic constants were not influenced by a 10 *T* magnetic field. This means that the Gibbs free energy is not influenced by a high magnetic field (B < 10 *T*). As we know, the Gibbs free energy is closely related to both undercooling and supersaturation.[49] A large temperature gradient and cooling rate increase undercooling and promote the nucleation of the γ' phase.[14,49,50] However, during directional solidification, the cooling rate V depends on the temperature gradient G and the growth rate of dendrites R; that is, $V = G \times R$.[5,8,12] According to Li *et al.*,[52] the growth rate of dendrite R is related to the undercooling ΔT during directional solidification as $R \propto (\Delta T)^b$, where b is a constant. Therefore, the relation between cooling rate and undercooling can be expressed as $V \propto (\Delta T)^b$, which means that the cooling rate increases with undercooling (ΔT). Recently, Nguyen-Thi *et al.*[53] showed that convection increases constitutional undercooling in front of the solid/liquid interface. This implies that convection of the melt can cause cooling rate to increase during directional solidification. As a consequence, undercooling increases, promoting the

nucleation of the γ' phase based on the above analyses and phase transformation theory. Similarly, when a magnetic field is applied during directional solidification, TEMC causes cooling rate to increase, which increases the undercooling of the γ' phase and promotes the nucleation of this phase. In addition, the growth time of the γ' phase is decreased because of the refined primary dendrite arm spacing in a high magnetic field. As a consequence, refined γ' phases are formed during directional solidification in a high magnetic field. Therefore, the interdendritic TEMC in the magnetic field should be responsible for the decrease of the size of the γ' phase.

During the directional solidification of superalloys, the γ/γ' eutectic is formed in the interdendritic region during the final stage of solidification because of the solute segregation of Al, Ti, and Ta in this region. Therefore, the degree of solute segregation is a major factor that affects the size and number of γ/γ' eutectic. An investigation indicates that the melt flow affects the distribution of the solute during directional solidification.[54] Similarly, TEMC induced by a high magnetic field promotes melt flow in the interdendritic region and decreases the degree of solute segregation (the enrichment of solute) when a magnetic field is applied; consequently, the size and number of γ/γ' eutectic are decreased.

To confirm the effect of TEMC on solute segregation during the solidification process in a high magnetic field, the distributions of the solutes in the dendrite core and interdendritic region were investigated. The segregation of elements is described by the element segregation coefficient k', which is $k' = C_D/C_i$, where C_D is the average concentration of each element in the dendrite core and C_i is the average concentration of each element in the interdendritic region. If $k' = 1$, the elements are homogeneously distributed in the dendrite core and interdendritic region of a sample. When $k' > 1$, the elements are negative segregation elements that are

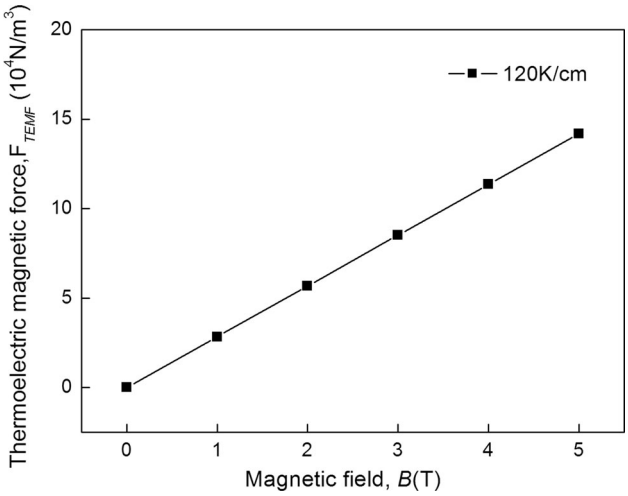

Fig. 6—Thermoelectric magnetic force of dendrites as a function of magnetic field intensity B.

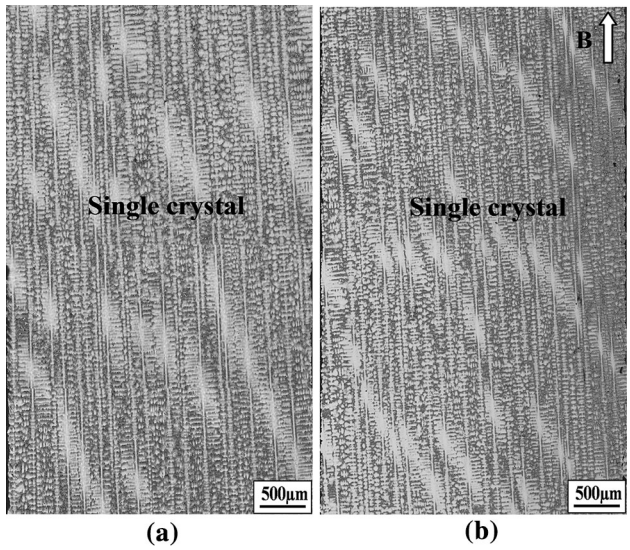

Fig. 7—Longitudinal microstructures near the solid–liquid interface in the directionally solidified superalloy PWA1483 (*a*) without and (*b*) with a 5 T magnetic field (v = 50 μm/s).

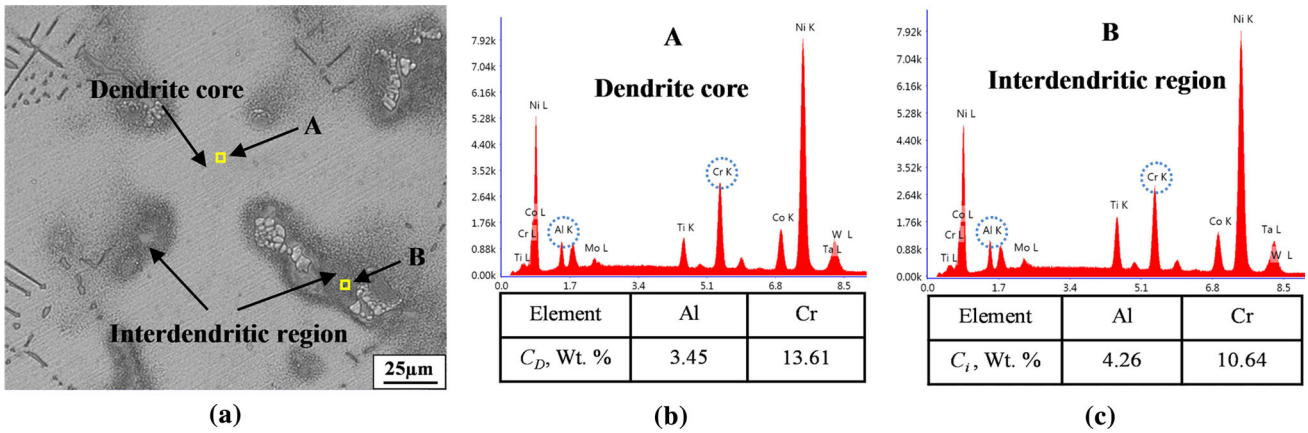

Element	Al	Cr
C_D, Wt. %	3.45	13.61

Element	Al	Cr
C_i, Wt. %	4.26	10.64

Fig. 8—Distributions of Al and Cr in the dendrite core and interdendritic regions measured by energy-dispersive X-ray spectroscopy (EDS). (*a*) Scanning areas of EDS. Distributions of Al and Cr in the (*b*) dendrite core and (*c*) interdendritic region (region A and B, respectively, in (a)).

Table IV. Average Element Concentration of Superalloy PWA1483

	Average Concentration of Element (Wt Pct)			
	0 *T*		5 *T*	
Element	C_D	C_i	C_D	C_i
Al	3.45	4.26	3.54	3.73
Ti	3.42	5.56	3.63	4.65
Ta	4.29	5.84	4.56	5.37
Cr	13.02	10.06	12.45	11.53
Co	9.54	8.37	9.19	8.92
W	4.34	3.55	4.14	3.71

Table V. Average Element Concentration of Superalloy CMSX-4

	Average Concentration of Each Element (Wt Pct)			
	0 *T*		5 *T*	
Element	C_D	C_i	C_D	C_i
Al	5.18	6.9	5.47	5.93
Ta	5.44	7.75	5.86	7.41
Cr	7.62	5.77	6.45	6.58
Co	9.71	8.02	9.32	8.61
W	7.08	5.45	6.39	5.56
Re	3.92	2.42	3.46	2.79

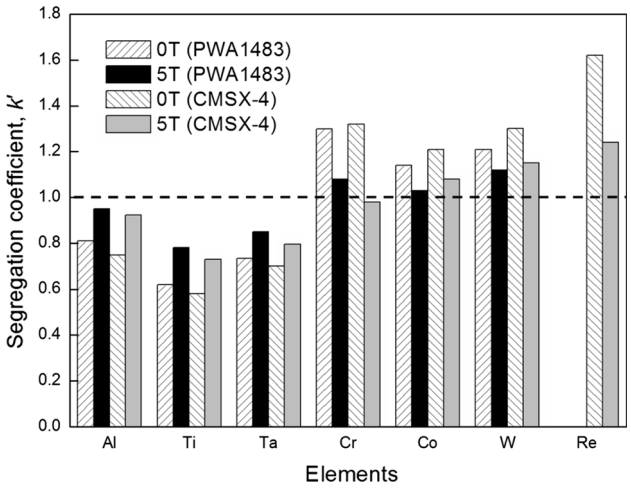

Fig. 9—Segregation coefficients of alloy elements in the superalloy PWA1483 and CMSX-4 samples produced without and with a 5 *T* magnetic field.

enriched in the dendrite core; if $k' < 1$, the elements are positive segregation elements that are enriched in the interdendritic region. Here, k' is used to explain the segregation of the dendrite core and the interdendritic region. The distribution of Al and Cr in the dendrite core and interdendritic regions is shown in Figure 8. According to $k' = C_D/C_i$, elements segregation coefficients k_{Al}' and k_{Cr}' of about 0.81 and 1.3, respectively, were obtained.

Tables IV, V, and Figure 9 show the segregation behaviors of superalloys PWA1483 and CMSX-4 without and with a 5 *T* magnetic field. Compared with the case with no magnetic field, a 5 *T* magnetic field decreased the degree of solute segregation in the dendrite core and interdendritic region. This means that the TEMC induced by a high magnetic field decreases the degree of solute segregation and further decreases the size and number of γ/γ' eutectic under the current experimental conditions. Moreover, the refined primary dendrite arm spacing decreases the solute segregation in the interdendritic region, and then the size and volume faction of γ/γ' eutectic are decreased. Therefore, the decrease of the size and volume faction of γ/γ' eutectic should also be attributed to the interdendritic TEMC induced by the high magnetic field during directional solidification.

V. CONCLUSIONS

The effects of a high magnetic field on the microstructures formed during directional solidification of Ni-based single-crystal superalloys PWA1483 and CMSX-4 were investigated. The primary dendrite arm spacing, size of the γ' phase, and microsegregation were modified in a high magnetic field. Moreover, the high magnetic field decreased the size and volume fractions of γ/γ' eutectic and microporosity of PWA1483 and CMSX-4. ANOVA analyses showed that the high magnetic field significantly affected the microstructures of both PWA1483 and CMSX-4. Our results revealed that the formation of interdendritic TEMC in a high magnetic field should be responsible for the refinement of primary dendrite arm spacing, decrease of the size of

the γ' phase, and decrease of the size and volume fraction of γ/γ' eutectic and microporosity during directional solidification of superalloys PWA1483 and CMSX-4.

ACKNOWLEDGMENTS

This work was financially supported by the Natural Science Foundation of China (Nos. 51604172, 51401116, U1560202) and the Shanghai Municipal Education Commission.

REFERENCES

1. N. D'Souza, P.A. Jennings, X.L. Yang, H.B. Dong, P.D. Lee, and M. McLean: *Metall. Mater. Trans. B*, 2005, vol. 36, pp. 657–66.
2. M. McLean: *Directionally Solidified Materials for High Temperature Service*, The Metals Society, London, 1983, pp. 161–63.
3. F. Wang, D.X. Ma, Y.R. Mao, S. Bogner, and A. Bührig-Polaczck: *Metall. Mater. Trans. B*, 2016, vol. 47, pp. 76–84.
4. A.J. Elliott, S. Tin, W.T. King, S.C. Huang, M.F.X. Gigliotti, and T.M. Pollock: *Metall. Mater. Trans. A*, 2004, vol. 35, pp. 3221–31.
5. L. Liu, T.W. Huang, J. Zhang, and H.Z. Fu: *Mater. Lett.*, 2007, vol. 61, pp. 227–30.
6. D.X. Ma and A. Bührig-Polaczck: *Metall. Mater. Trans. B*, 2009, vol. 40, pp. 738–48.
7. M. Konter and M. Thumann: *J. Mater. Process. Technol.*, 2001, vol. 117, pp. 386–90.
8. T.M. Pollock and W.H. Murphy: *Metall. Mater. Trans. A*, 1996, vol. 27A, pp. 1081–94.
9. J.P. Gu, C. Beckermann, and A.F. Giamei: *Metall. Mater. Trans. A*, 1997, vol. 28A, pp. 1533–42.
10. C.L. Brundidge, D. Vandrasek, B. Wang, and T.M. Pollock: *Metall. Mater. Trans. A*, 2012, vol. 43A, pp. 965–76.
11. J. Zhang and L.H. Lou: *J. Mater. Sci. Technol.*, 2007, vol. 23, pp. 289–99.
12. X.B. Zhao, L. Liu, Z.H. Yu, W.G. Zhang, J. Zhang, and H.Z. Fu: *J. Mater. Sci.*, 2010, vol. 45, pp. 6101–07.
13. M. Konter, E. Kats, and N. Hofmann: in *Superalloys*, T.M. Pollock, R.D. Kissinger, R.R. Bowman, K.A. Green, M. McLean, S.L. Olson, and J.J. Schirra, eds., TMS, Warrendale, 2000, pp. 189–200.
14. F. Wang, D.X. Ma, J. Zhang, L. Liu, J. Hong, S. Bogner, and A. Bührig-Polaczck: *J. Cryst. Growth*, 2014, vol. 389, pp. 47–54.
15. R.T. Holt and W. Wallace: *Int. Meter. Rev.*, 1976, vol. 21, pp. 1–24.
16. X.B. Meng, J.G. Li, Z.Q. Chen, Y.H. Wang, S.Z. Zhu, X.F. Bai, F. Wang, J. Zhang, T. Jin, X.F. Sun, and Z.Q. Hu: *Metall. Mater. Trans. A*, 2013, vol. 45A, pp. 1955–65.
17. D. Ma, H. Lu, and A. Bührig-Polaczck: *IOP Conf. Ser. Mater. Sci. Eng.*, 2012, vol. 27, p. 012036.
18. Y.D. Zhang, C. Esling, M.L. Gong, G. Vincent, X. Zhao, and L. Zuo: *Scr. Mater.*, 2006, vol. 54, pp. 1897–1900.
19. P. Lehmann, R. Moreau, D. Camel, and R. Bolcato: *J. Cryst. Growth*, 1998, vol. 183, pp. 690–94.
20. X. Li, Y. Fautrelle, and Z.M. Ren: *Acta Mater.*, 2008, vol. 56, pp. 3146–61.
21. W.V. Youdelis and R.C. Dorward: *Can. J. Phys.*, 1966, vol. 44, pp. 139–50.
22. C. Vives and C. Perry: *Int. J. Heat Mass Tran*, 1986, vol. 29, pp. 21–33.
23. T. Zhang, W.L. Ren, J.W. Dong, X. Li, Z.M. Ren, G.H. Cao, Y.B. Zhong, K. Deng, Z.S. Lei, and J.T. Guo: *J. Alloys Compd.*, 2009, vol. 487, pp. 612–17.
24. W.L. Ren, T. Zhang, Z.M. Ren, A.K. Zhao, Y.B. Zhong, and J.T. Guo: *Mater. Lett.*, 2009, vol. 63, pp. 223–26.
25. W.D. Xuan, Z.M. Ren, and C.J. Li: *J. Alloys Compd.*, 2015, vol. 621, pp. 10–17.
26. W.D. Xuan, Z.M. Ren, C.J. Li, W.L. Ren, C. Chen, and Z. Yu: *Acta Metall Sin.*, 2012, vol. 48, pp. 629–35.
27. X. Li, A. Gagnoud, Z.M. Ren, Y. Fautrelle, and R. Moreau: *Acta Mater.*, 2009, vol. 57, pp. 2180–97.
28. H.S. Whitesell, L. Li, and R.A. Overfelt: *Metall. Mater. Trans. B*, 2000, vol. 31, pp. 546–51.
29. C. Vives and C. Perry: *Int. J. Heat Mass Transf.*, 1987, vol. 30, pp. 479–96.
30. W.E. Langlois and K.J. Lee: *J. Cryst. Growth*, 1983, vol. 62, pp. 481–86.
31. W.D. Xuan, Z.M. Ren, and C.J. Li: *Metall. Mater. Trans. A*, 2015, vol. 46A, pp. 1461–66.
32. W.J. Boettinger, F.S. Biancaniello, and S.R. Coriell: *Metall. Mater. Trans. A*, 1981, vol. 12A, pp. 321–27.
33. P. Lehmann, R. Moreau, D. Camel, and R. Bolcato: *Acta Mater.*, 1998, vol. 46, pp. 4067–79.
34. S. Yesilyurt, L. Vujisic, S. Motakef, F.R. Szofran, and M.P. Volz: *J. Cryst. Growth*, 1999, vol. 207, pp. 278–91.
35. X. Li, Y. Fautrelle, and Z.M. Ren: *Acta Mater.*, 2007, vol. 55, pp. 3803–13.
36. Y.Y. Khine and S. Walker: *J. Cryst. Growth*, 1998, vol. 183, pp. 150–58.
37. P. Dolda, F.R. Szofranb, and K.W. Benz: *J. Cryst. Growth*, 2006, vol. 291, pp. 1–7.
38. H. Yasuda, T. Yoshimoto, T. Mizuguchi, Y. Tamura, T. Nagira, and M. Yoshiya: *ISIJ Int.*, 2007, vol. 47, pp. 612–18.
39. G. Pottlacher, H. Hosaeus, B. Wilthan, E. Kaschnitb, and A. Seifter: *Thermochim. Acta*, 2002, vol. 382, pp. 255–67.
40. X. Li, Y. Fautrelle, K. Zaidat, A. Gagnoud, Z.M. Ren, R. Moreau, Y.D. Zhang, and C. Esling: *J. Cryst. Growth*, 2010, vol. 312, pp. 267–72.
41. M.D. Dupouy, D. Camel, and J.J. Favier: *Acta Metall Mater*, 1992, vol. 40, pp. 1791–1801.
42. S. Steinbach and L. Ratke: *Metall. Mater. Trans. A*, 2007, vol. 38A, pp. 1388–94.
43. J. Hui, R. Tiwari, X. Wu, S.N. Tewari, and R. Trivedi: *Metall. Mater. Trans. A*, 2002, vol. 33A, pp. 3499–3510.
44. K.A. Jackson, J.D. Hunt, D.R. Uhlmann, and T.P. Seward: *Trans. TMS–AIME*, 1966, vol. 236, pp. 149–58.
45. J. Lipton, M.E. Glicksman, and W. Kurz: *Mater. Sci. Eng.*, 1984, vol. 65, pp. 57–63.
46. M. Rappaz and Ch.-A. Gandin: *Acta. Metall. Mater.*, 1993, vol. 41, pp. 345–60.
47. P.A. Curreri, J.E. Lee, and D.M. Stefanescu: *Metall. Trans, A*, 1988, vol. 19, pp. 2671–76.
48. D.R. Poirier, K. Yeum, and A.L. Maples: *Metall. Trans. A*, 1987, vol. 18A, pp. 1979–87.
49. J.M. Xiao: *Alloy Phase and Its Transformation*, The Chinese Metallurgical Publishing House, Beijing, 1987, pp. 233–35.
50. X.P. Guo, H.Z. Fu, and J.H. Sun: *Metall. Trans. A*, 1997, vol. 28A, pp. 997–1009.
51. M. Yamaguchi and Y. Tanimoto: *Magneto-Science*, Springer, Berlin, 2006, pp. 15–17.
52. C.J. Li, Z.M. Ren, and W.L. Ren: *IOP Conf. Ser.: Mater. Sci. Eng.*, 2011, vol. 27, p. 012052.
53. L. Abou-Khalil, G. Salloum-Abou-Jaoude, G. Reinhart, C. Pickmann, G. Zimmermann, and H. Nguyen-Thi: *Acta Mater.*, 2016, vol. 110, pp. 44–52.
54. X. Li, Y. Fautrelle, A. Gagnoud, D. Du, J. Wang, Z. Ren, H. Nguyen-Thi, and N. Mangelinck-Noel: *Acta Mater.*, 2014, vol. 64, pp. 367–81.